Available online at www.sciencedirect.com
ScienceDirect
Advances in Space Research 38 (2006) 1694–1701
ADVANCES IN SPACE RESEARCH (a COSPAR publication)
www.elsevier.com/locate/asr

The anisotropy of precipitating auroral electrons: A FAST case study

O. Marghitu [a,b,*], B. Klecker [b], J.P. McFadden [c]

[a] Institute for Space Sciences, RO-77125 Bucharest, Romania
[b] Max-Planck-Institut für extraterrestrische Physik, D-85748 Garching, Germany
[c] Space Sciences Laboratory, University of California at Berkeley, CA 94720, USA

Received 30 October 2004; accepted 26 March 2006

Abstract

A key component in the magnetosphere–ionosphere coupling chain is the auroral acceleration region (AAR), where electromagnetic energy is converted into kinetic energy of precipitating electrons. We examine the accelerated electrons measured by FAST during an auroral overpass when the spacecraft crosses the AAR several times, as evident from the observation of ion beams. We assume that above the AAR the electron population is bi-Maxwellian and fit accelerated bi-Maxwellian functions to the measured distributions. When the electron motion between the plasma sheet source and the satellite can be considered as adiabatic, two of the fit parameters can be associated with the source properties, while the third one provides the electron anisotropy profile along the satellite track; the fit quality parameter, χ_r^2, gives an indication about the importance of non-adiabatic processes. We explore the possibility of using the anisotropy to determine the altitude of the AAR top boundary (AARTB) and find that when the AAR bottom boundary (AARBB) is located closer to the Earth, as proved by the detection of ion beams, the AARTB appears to be pushed at higher altitudes. This fact is discussed with regard to recent theoretical and experimental results.

Keywords: Magnetosphere–ionosphere interaction; Auroral acceleration region; Particle precipitation; Bi-Maxwellian distribution; Electron anisotropy

1. Introduction

The precipitating auroral electrons gain most of their energy within the AAR, where the electromagnetic energy is transformed into particle kinetic energy, by means of an electric field, $E_\parallel$, parallel to the geomagnetic field. The AAR develops as an interface that decouples the hot and tenuous magnetospheric plasma from the cold and dense ionospheric plasma. Shortly after Alfvén (1958) predicted the $E_\parallel$ in the plasma around the Earth, McIlwain (1960) reported the first experimental evidence for its existence, based on rocket electron data.

The location of the AAR was discovered later, 'almost accidentally' (cf. Fälthammar, 1983), by the satellite S3-3. Equipped with a complete set of particle and field instruments, S3-3 provided the first systematic AAR in situ database and allowed for the 'drawing' of the first AAR 'map' (e.g., Mizera et al., 1981). The results obtained by S3-3 were confirmed and detailed by missions like Dynamics Explorer, Viking, Freja, and FAST. Up to date information and references concerning the aurora and the AAR can be found e.g., in Lindqvist (2001) and Paschmann et al. (2003).

Particle data were instrumental for the investigation of the AAR since the pioneering paper of McIlwain (1960). Electron and ion spectrometers as the ones flown on S3-3 gave the possibility of a detailed study of the 2D distribution function, in a plane that includes the magnetic field line, with a time resolution equal to the satellite spin period. The S3-3 heritage was developed on FAST, the second NASA Small Explorer satellite, launched on August 21, 1996, in a polar orbit (83°), apogee/perigee at 4200/380 km, whose primary goal was to investigate the

* Corresponding author. Tel.: +40 21 457 4131; fax: +40 21 457 4471.
E-mail addresses: marghitu@venus.nipne.ro (O. Marghitu), berndt.klecker@mpe.mpg.de (B. Klecker), mcfadden@ssl.berkeley.edu (J.P. McFadden).

0273-1177/$30
doi:10.1016/j.asr.2006.03.028

small scale structure of the AAR (Pfaff et al., 2001, and references therein). Due to an innovative design the electron (EESA) and ion (IESA) spectrometers (Carlson et al., 2001) offer an 'instantaneous' 360° field-of-view in a plane including the magnetic field line, which results in about two orders of magnitude better time resolution, compared to previous missions.

This paper aims to develop a remote sensing tool, based on particle data measured by FAST during AAR crossings, and able to provide information on the parameters of the plasma above the AAR, as well as on the location of the AARTB. In order to achieve this goal we shall use data measured during a winter nightside auroral overpass, that will be introduced in Section 2. We will continue in Section 3 with a discussion of the electron distribution function and a brief description of the procedure developed for fitting measured distributions to analytical forms. After presenting the fit results in Section 4 we will explore the possibility to use them in order to derive the altitude of the AARTB in Section 5.

2. FAST orbit 1859: data

We shall concentrate below on particle data measured by FAST above the auroral oval on February 9, 1997, 8:22–8:23 UT, at 3850 km altitude and 21 MLT. At the same time conjugated optical data were recorded with a ground TV camera, located at Deadhorse, in northern Alaska (Lat. 70.22°, Lon. 211.61°). The low-light CCD camera, developed at Max-Planck-Institut für extraterrestrische Physik, Garching (Frey et al., 1996), was equipped with wide-angle optics ($86° \times 64°$) and a $\geqslant 650$ nm passband filter. The optical data show a wide ($\sim$70 km), stable, and moderately bright arc. Fig. 1 presents the two frames recorded at the beginning and the end of the interval under study.

The visible arc is embedded in a large inverted-V, as seen in the top panel of Fig. 2. Its most energetic part (peak energy $W_A \lesssim 5$ keV, and energy flux $J_W \lesssim 10\text{mW/m}^2$) was measured above the arc. The inverted-V encompasses several ion beams (mid panel of Fig. 2), a typical signature

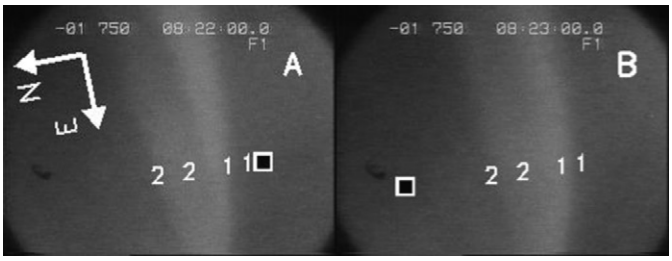

Fig. 1. Ground images at 8:22:00 (A) and 8:23:00 (B), the time limits of the interval under study. Except for an 200 m/s southward drift, the arc remains stable during this interval. FAST ionospheric footprint is shown as a square (mapping courtesy Dr. Joachim Vogt). '11' and '22' are the limits of the first two ion beams; placing beams' markers in the two frames is meant to provide a reference for the luminosity evolution and does not imply that the beams are necessarily there.

for the FAST winter apogee passes above the northern oval, from January–February 1997. The electron and ion data are consistent with repeated encounters of the AAR, which behaves as a quasi-static potential structure on the satellite crossing time scale of $\sim$10 s (e.g., McFadden et al., 1999). The peak energy of the field-aligned (FA) precipitating electrons, W_A, and upgoing beam ions, W_B, provide proxies for the FA potential drop above and below the satellite, respectively (bottom panel of Fig. 2). We note that, as measured by the mass spectrometer TEAMS (Klumpar et al., 2001) and in agreement with the relatively quiet auroral conditions, the ion beams consist mainly of H^+ (not shown).

3. Electron distributions and fit procedure

A more detailed view over the electron precipitation is offered by the examination of the 2D distribution function. In the following we shall use Survey data, with a time resolution of 312 ms, comprising 48 logarithmically spaced energy channels in the range 4 eV–35 keV, and 64 angular channels of 5.6° each. After a qualitative exploration, we shall discuss the possibility to fit an analytic function to the measured data and briefly describe the routine which performs the fit.

3.1. Electron distributions

Fig. 3a shows a selection of 4 electron distributions, measured on field lines that map both inside and outside of the visible arc. A complementary view is offered by the spectra in Fig. 3b, which represent sections through the distribution functions in parallel, anti-parallel, and perpendicular direction, with respect to the magnetic field.

The distribution function exhibits a plateau in parallel direction, at energies $W \lesssim W_A$, which indicates wave–particle interactions tending to stabilize the accelerated distribution; this feature is prominent above the visible arc. At energies higher than W_A the distribution function decreases roughly linear in the log-linear plots, which is consistent with an exponential dependence on energy. In addition, the contour plots are roughly elliptical for precipitating electrons with energies $W > W_A$, which suggests the bi-Maxwellian function:

$$f_M = K \times \frac{n_M}{A_M W_{0_{\|M}}^{3/2}} \times \exp\left[-\left(\frac{W_{\|M}}{W_{0_{\|M}}} + \frac{W_{\perp M}}{A_M W_{0_{\|M}}}\right)\right] \qquad (1)$$

as a reasonable analytic form to fit the measured distributions, at energies above W_A and in downward direction ($v_\| > 0$). In Eq. (1), $K = (m/2\pi)^{3/2}$, n_M is the density, $W_{0_{\|M}}$ the parallel temperature, $A_M = W_{0_{\perp M}}/W_{0_{\|M}}$ the anisotropy, and M indicates quantities at the measuring location.

Eq. (1) can be expressed in terms of the plasma sheet source parameters, assuming that: (i) the particle distribution there is bi-Maxwellian, and (ii) the particle motion

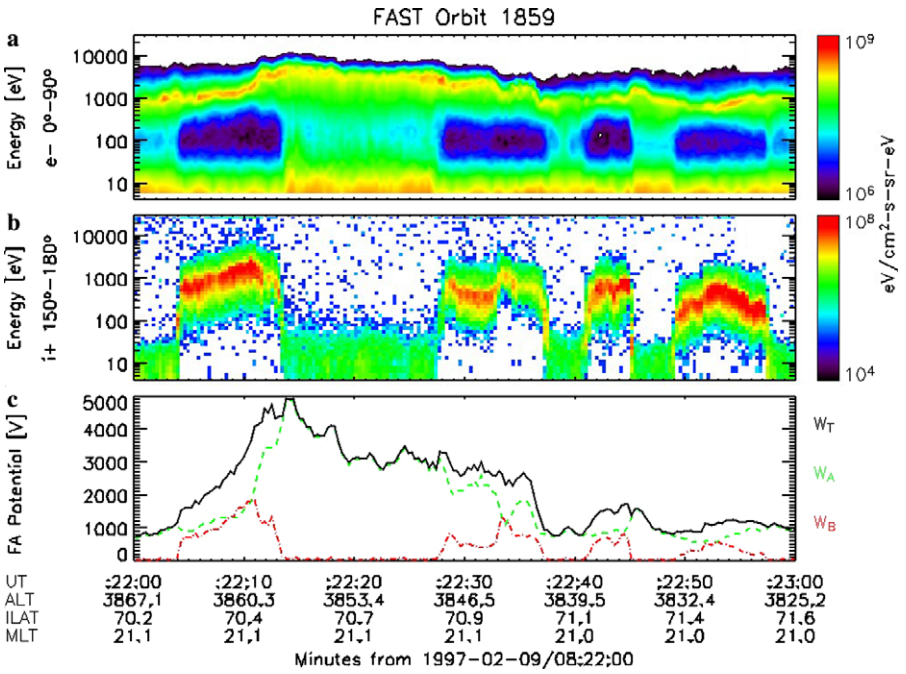

Fig. 2. FAST particle data, consistent with repeated encounters of the AAR. (a and b) Electron and ion energy spectrograms; (c) field-aligned potential drop above the satellite (green dashes), below the satellite (red dash-dots) and total (black solid), derived from electron and ion peak energies. Detailed electron data, for the times indicated by vertical lines, are presented in Fig. 3.

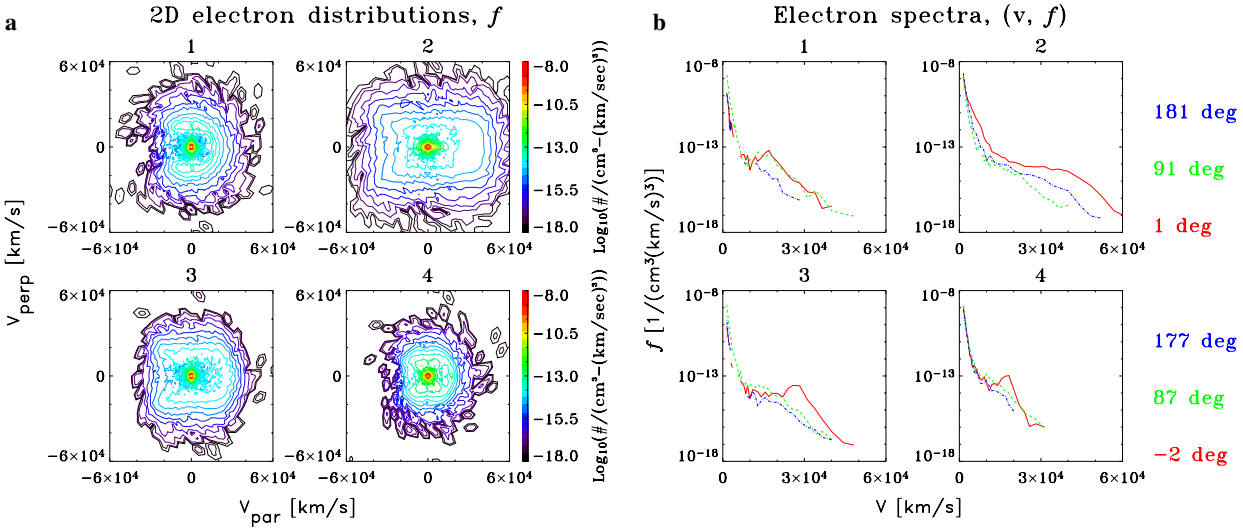

Fig. 3. Selection of electron Survey distributions, measured on field lines that map outside (1 and 4), and inside (2 and 3) the visible arc; the respective times are indicated with vertical lines in Fig. 2. (a) 2D distribution functions, in $1/cm^3$ $(km/s)^3$ units. (b) 1D cuts in parallel (red solid), perpendicular (green dashes), and anti-parallel (blue dash-dots) direction.

between the 'source' and satellite is adiabatic. Assumption (i) takes into account the anisotropy introduced by the magnetic field, while (ii) is worth checking, in particular for a wide arc as ours. As found by many experiments, starting with Lyons et al. (1979), for wide arcs the current carried by precipitating particles into the ionosphere is proportional to the field-aligned potential drop, $I = KU$, a relationship consistent with an adiabatic particle motion (Knight, 1973). One cannot expect that the particle motion is rigorously adiabatic but, considering the large amount of experimental evidence, one may hope that the 'memory' of the source population is preserved, to some extent, down to the satellite location.

If the plasma sheet electrons are bi-Maxwellian the source distribution function, f_S, written as in Eq. (1), except for the index M which is changed to S. By using the energy conservation

$$W_{\parallel S} + W_{\perp S} = W_{\parallel M} + W_{\perp M} - W_A \tag{2}$$

the adiabatic condition

$$W_{\perp S} = W_{\perp M}/r, \quad r = B_M/B_S = \text{measured } B/\text{source } B \quad (3)$$

and the fact that the plasma is collisionless, which implies $f_M = f_S$, the distribution function of the precipitating plasma sheet electrons, at the measuring location, can be written as:

$$f_M = K \times \frac{n_S}{A_S W_{0_\parallel S}^{3/2}} \times \exp\left[-\left(\frac{W_{\parallel M} - W_A}{W_{0_\parallel S}} + \frac{W_{\perp M}}{A_M W_{0_\parallel S}}\right)\right] \quad (4)$$

with $W_{0_\parallel S} = W_{0_\parallel M}$ and A_M given by:

$$A_M = \frac{1}{1 - \frac{1}{r}\frac{A_S - 1}{A_S}}. \quad (5)$$

3.2. Fit procedure

The fit of the analytic function Eq. (4) to the measured electron distributions yields the mathematical parameters:

$$p_1 = K \times \frac{n_S}{A_S} \times \frac{\exp(W_A/W_{0_\parallel S})}{W_{0_\parallel S}^{3/2}}$$
$$p_2 = W_{0_\parallel S}$$
$$p_3 = A_M W_{0_\parallel S}. \quad (6)$$

By inverting the system (6) one finds the physical parameters n_S/A_S, $W_{0_\parallel S}$ and A_M. In order to perform the computations we developed the IDL^R routine *AURFIT*, which finds the minimum of the χ^2 type expression:

$$h = \sum_{W_{\inf}}^{W_{\sup}} \sum_{\theta_{\inf}}^{\theta_{\sup}} \frac{[\text{data}(W_i, \theta_j) - f(W_i, \theta_j, p_1, p_2, \ldots)]^2}{\sigma^2_{\text{data}}(W_i, \theta_j)}. \quad (7)$$

The analytic function f can take any form indicated by the user, depending on the parameter set $(p_1, p_2, \ldots)$; the energy range, $[W_{\inf}, W_{\sup}]$, as well as the pitch-angle range, $[\theta_{\inf}, \theta_{\sup}]$, can be set at will. The square error, σ^2, is computed from the measured data and is proportional to the count number. In order to improve the reliability of the results *AURFIT* can check several starting points in the parameter space, which reduces the probability that the minimization algorithm finds just a local minimum of the non-linear function h. Once the minimum is found, *AURFIT* computes the reduced χ^2

$$\chi^2_r = \frac{\chi^2}{N - P},$$
$$N = \text{no. of energy-angle bins},$$
$$P = \text{no. of parameters} \quad (8)$$

which measures the fit quality. In the next section we will present and discuss fit results obtained with the accelerated bi-Maxwellian function, Eq. (4).

4. FAST orbit 1859: results

We performed the fit on all the 192 Survey electron distributions measured between 8:22 and 8:23 UT. For each distribution we used the first seven energy levels above the peak energy, $W \geqslant W_A$, a pitch-angle range $\theta \leqslant 90°$, and 10 different starting values for each parameter, amounting to a total of 1000 starting points in the parameter space for each electron distribution.

The results of the fit are presented in Fig. 4. Panel (a) shows $\chi^2_{r_{\min}}$, the minimum χ^2_r found among the values obtained with different starting points. In order to check whether there is any relationship between the fit quality and the potential drop above the satellite, the scaled profile of W_A is overplotted. One notes that $\chi^2_{r_{\min}} \lesssim 5$ before 8:22:10 and after 8:22:40, when W_A is reduced, but goes up to ~20 when W_A is substantial. This is consistent with the expectations: for a higher accelerating potential the distribution becomes more unstable and deviates more from bi-Maxwellian.

The physical parameters $(n_S/A_S, W_{0_\parallel M}, W_{0_\perp M})$ obtained by fit, together with the anisotropy, $A_M = W_{0_\perp M}/W_{0_\parallel M}$, are presented in the panels (b–e); the scaled profile of W_B is overplotted in panel (e), to ease the examination of the anisotropy versus the alternation of ion beams.

The parameter values are in good agreement with the experimental data. In a recent statistical study based on 93 Polar orbits Kletzing et al. (2003) found plasma sheet electron densities and temperatures above the AAR of 0.01–0.5 cm^{-3} and 100–4000 eV, with averages at 0.1 cm^{-3} and 400 eV above the poleward side of the auroral oval. The correlation between the temperature and the FA potential drop, visible in Fig. 4, was observed already in DE data, by Reiff et al. (1988), who found that the electron temperature is equal to about 10–15% of the FA potential drop. This suggests non-adiabatic heating processes, that cannot be disregarded above the visible arc, between about 8:22:10 and 8:22:40.

A feature worth mentioning is that the plasma sheet parameters do not change too much: there is neither an increasing nor a decreasing trend in n_S/A_S, while the parallel temperature keeps about the same value on both sides of the visible arc and its variation seems to be related just to the FA potential drop. During the 1960s investigated, FAST travels 330 km, that map to ~1000 km in the source plasma sheet, assuming that the AARTB is not higher than a few R_E. It is reasonable that, on such a scale, the plasma sheet parameters have little variation.

Quite interesting in Fig. 4 is the evolution of the anisotropy. If we focus only on the time outside the visible arc, which includes most of the first, as well as the third and the forth ion beams, one notes a tendency of $A_M < 1$ for the intervals outside, and $A_M \simeq 1$ inside the beams. Inside the visible arc one does also see a small increase in the anisotropy at 8:22:27, the left boundary of the second ion beam.

Before proceeding to next section we want to shortly comment on our choice of the fit function, the anisotropic Maxwellian, versus the usual choice, the isotropic Maxwellian. The results obtained with isotropic Maxwellian (not shown), both the fit quality, χ^2_r, and the parameters, density and temperature (n, W_0), are pretty similar to

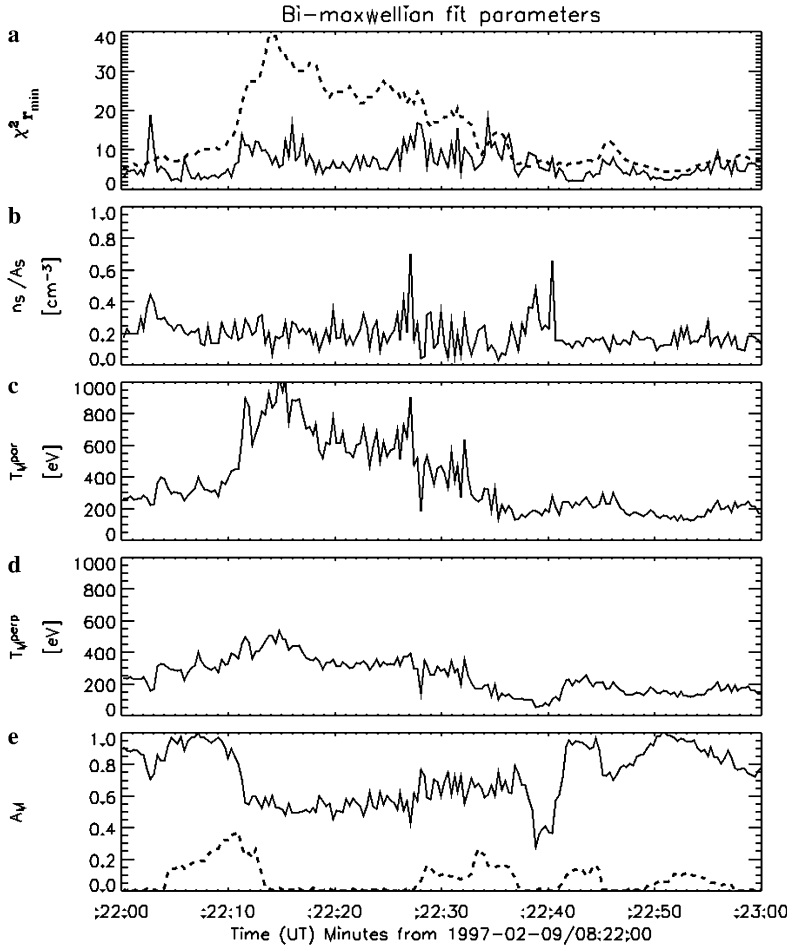

Fig. 4. (a) Fit quality parameter, $\chi^2_{r_{min}}$. (b–e) Fit parameters: density, parallel and perpendicular temperature, anisotropy. The scaled profiles of the potential drop above and below the satellite are overplotted with dashes in the top and bottom panels, respectively.

those presented in Fig. 4 (the average temperature for the anisotropic Maxwellian was computed as $W_0 = (W_{0_\parallel} + 2W_{0_\perp})/3$). Nevertheless, the fit with isotropic Maxwellian misses the information carried by anisotropy which, as discussed below, can prove to be useful.

5. Electron anisotropy and AAR altitude

The altitudinal extension of the AAR was investigated by both statistical and case-study means, using ion data for the location of the AARBB (e.g., Gorney et al., 1981; Lu et al., 1992; Temerin et al., submitted for publication), and electron data for the location of the AARTB (e.g., Fennell et al., 1981; Reiff et al., 1993). Here we discuss the possible relationship between the anisotropy and the ion beam sequence, and then develop a quantitative method which, under certain conditions, might be used to evaluate the altitude of the AARTB.

We assume one can speak about the 'boundaries' of the AAR, i.e., these boundaries are relatively narrow in altitude, as suggested by experimental (e.g., McFadden et al., 1999; Mozer and Hull, 2001) and simulation (e.g., Ergun et al., 2000; Gurgiolo and Burch, 1988) studies. This assumption is consistent with the fact that different plasmas, as in the ionosphere, AAR, and plasma sheet, tend to be separated by narrow layers that concentrate relatively large potential drops.

The possibility to use the iso-density contours of the electron distribution function in the ($v_\parallel$, $v_\perp$) space, in order to find the FA potential variation, was explored by e.g., Kaufmann et al. (1976), using rocket data, and Fennell et al. (1981), using satellite data. The way the iso-density contours change depends on the exact variation of the magnetic field and electric potential between the 'source' and the measuring point. In addition, the variation of the electric potential influences the 'boundaries' in the velocity space (visible as 'kinks' in the iso-density contours), if several populations of different origins are present (like precipitating, backscattered, and secondaries). The inconveniency of using the iso-density contours is that comparing the real data to simulated distributions is rather qualitative (as in Kaufmann et al., 1976), or requires both a reference and the current distribution (as in Fennell et al., 1981).

An alternative option is to use the anisotropy, as described in the following. Although this one parameter does not carry as much information as the distribution function, both a qualitative evaluation and a quantitative

estimate, based only on the current distribution, are possible, with potential for later systematic studies.

5.1. Qualitative evaluation

We shall start from Eq. (5), which relates the measured anisotropy, A_M, to the source anisotropy, A_S. By a careful inspection of Eq. (5) one can see that the sub- or supra-unitary character of the anisotropy is invariant: $A_M < 1$ if $A_S < 1$ and $A_M > 1$ if $A_S > 1$. When $A_S \approx 1$ (isotropic source distribution), and/or $r \gg 1$ (AARTB well above the satellite), $A_M \approx 1$: the distribution remains isotropic if it starts as isotropic, while if the distance to the AARTB is large, just the particles included in a narrow cone around the field line make it to the satellite, where they arrive expanded into a roughly isotropic distribution. If one assumes the non-adiabatic effects are of second order, $A_M \neq 1$ is indicative of an AARTB location not very far up above the satellite. At the same time, when $A_M \approx 1$ it is tempting to attribute it to an increase in the altitude of the AARTB (and not to a change of the distribution from anisotropic to isotropic).

In our case, as already discussed, the non-adiabatic effects are of second order only outside the visible arc. The tendency of the anisotropy there to raise up to ~1 during the beams and to decrease to <1 outside of the beams suggests a 'dilation' and 'contraction' of the AAR, as sketched in Fig. 5. Such a configuration is consistent with a simulation study of Ergun et al. (2000), who found that the AARBB consists of an 'electron transition layer', while the AARTB consists of an 'ion transition layer'; the bottom layer is located where the density of backscattered and secondary electrons is equal to the density of ionospheric ions; the top layer appears where the density of accelerated beam ions is equal to the density of magnetospheric ions; the altitude of the bottom layer depends on the FA current density and on the atmospheric scale height. Assuming this scenario is true, when the AARBB is located closer to the Earth, the source of ionospheric ions that fill the flux tube inside the AAR is more abundant. These ions dilute to magnetospheric densities at a higher altitude, which would explain the simultaneous expansion of the AAR both in downward and upward direction.

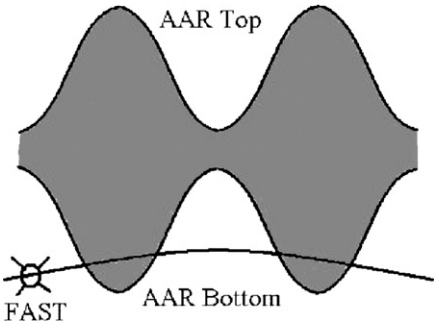

Fig. 5. Cartoon showing the 'dilation' and 'contraction' of the AAR. When the AARBB is located at low altitudes, below FAST, the AARTB is 'pushed' to higher altitudes.

5.2. Quantitative estimate

We return to Eq. (5) which, for $A_M \neq 1$, allows the derivation of r and, consequently, of the AARTB altitude, provided that A_S is known. Since the bi-Maxwellian fit yields

$$q^{\text{fit}} = n_S/A_S \tag{9}$$

one would get A_S once n_S is known. In order to estimate n_S we rely on Ergun et al. (2000), and adopt the suggestion that at AARTB the ion beam density, n_S^{IB}, is equal to the plasma sheet ion density, n_S^{PS}, which implies

$$n_S = 2n_S^{\text{IB}}. \tag{10}$$

If we further assume stationary conditions, with $J_M^{\text{IB}}/B_M = J_S^{\text{IB}}/B_S$ (J^{IB} is the ion beam flux), n_S^{IB} follows from

$$n_S^{\text{IB}} = J_S^{\text{IB}}/v_S^{\text{IB}} = J_M^{\text{IB}}/r\sqrt{2W_T/m_S^{\text{IB}}} \tag{11}$$

with m_S^{IB} the beam ion mass. By solving Eq. (5) with respect to r and introducing Eqs. (9)–(11), one finally obtains:

$$\frac{1}{r} = 1 - \frac{1}{A_M^{\text{fit}}} + \frac{q^{\text{fit}}}{2J_M^{\text{IB}}/\sqrt{2W_T/m_S^{\text{IB}}}} \tag{12}$$

which gives the expression of r in terms of measured and fitted quantities. Eq. (12) only applies for data collected inside the AAR, because of the approximation Eq. (10), used to estimate n_S. With r known, and assuming a dipole magnetic field (which is reasonable below 4–5R_E), the altitude of the AARTB above the satellite can be found from:

$$\Delta h = R_M(r^{1/3} - 1), \quad R_M = \text{the satellite geocentric distance.} \tag{13}$$

Fig. 6 shows results obtained with Eqs. (12) and (13) for the interval 8:22:04–8:22:14, when FAST crosses the first ion beam. During this time the satellite was in Burst mode and high resolution data are available (78 ms for a complete particle distribution); same as for the Survey data, the fit was performed over the downgoing part of the distribution, $\theta \leqslant 90°$. We assumed m_S^{IB} equal to the H^+ mass, in agreement with TEAMS data.

The most interesting feature is the increasing value of r (panel a) between 8:22:04 and 8:22:10, at the same time with the increase in the beam energy (panel d). This is consistent with an increase in the altitude of the AARTB (panel b) and with the qualitative picture from Fig. 5. During the last 4 s of the beam, when the ion energy drops down but the electron energy rises up, the fit quality (panel c) gets worse and the quantitative estimate becomes less useful.

Eq. (12) is quite sensitive to the errors in the involved quantities. Since the AARTB is above the satellite, $1 < r < \infty$, resulting in $0 < 1/r < 1$. When AARTB is high, $1/r$ is close to 0 and the errors in each of the parameters on the r.h.s. of Eq. (12) may lead to large fluctuations in r, between positive and negative values, as seen for the last 4 s of the beam in Fig. 6.

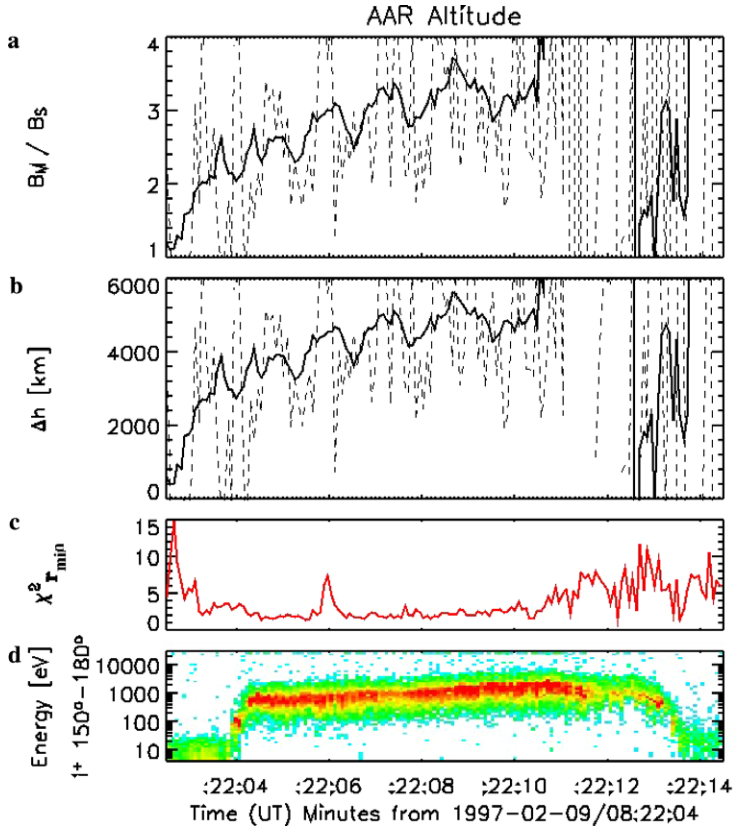

Fig. 6. (a and b) Magnetic field ratio, r (Eq. (12)), and altitude of the AARTB above the satellite, Δh (Eq. (13)), during the first ion beam; both actual (dashes) and smoothed (solid) profiles are plotted, in order to emphasize the trend. (c) Fit quality parameter, $\chi^2_{r_{\min}}$. (d) Ion energy spectrogram.

We tried to apply the same recipe for the second ion beam, between 8:22:27 and 8:22:37, when Burst data are again available. Not unexpected, we could not obtain reasonable results, presumably because the fit quality is not good enough, similar to the last part of the first ion beam (see Fig. 4a).

6. Summary and prospects

In the present paper, we developed a fit method which allows the remote diagnose of the plasma sheet electrons above the AAR. The method was checked with FAST data, measured around 3850 km altitude, and was found to yield densities and temperatures in good agreement with former Polar and DE results. The fit quality parameter, χ^2_r, seems to be related to the potential drop above the satellite and to provide an indication about the importance of non-adiabatic processes. The anisotropy of the precipitating electrons proved to be particularly interesting. It appears that this quantity carries information about the altitude of the AARTB which can be, to some degree, extracted. The case study we performed suggests that when the AARBB goes down to lower altitudes, the enrichment in ionospheric ions pushes the AARTB to higher altitudes.

The work can be continued by applying the same investigation method to other FAST orbits. More data is needed to explore the relevance of χ^2_r as a measure of the non-adiabatic processes, as well as the possibility to locate the AARTB by using the anisotropy of the precipitating electrons. The derived altitude of the AARTB depends on the heavy ion (He^+, O^+) content of the beam (influence on m^{IB}), as also on the finite energy step of the electron spectrometer (influence on W_A). This needs further study. In addition, in order to double check the ion density estimate at the AARTB, one could try to use both the beam ($150° \leqslant \theta \leqslant 180°$) and the mirrored plasma sheet ions ($90° \leqslant \theta \leqslant 150°$) measured by FAST.

Acknowledgements

O.M. acknowledges the hospitality and kind support of Max-Planck-Institut für extraterrestrische Physik, Garching, as well as useful discussions with R.J. Strangeway and J. Fennell. The work in Romania was funded through the programs CERES and AEROSPAŢIAL, Contracts 95/2001 PROFIS and 72/2003 PROSPERO.

References

Alfvén, H. On the theory of magnetic storms and aurorae. Tellus 10, 104–116, 1958.

Carlson, C., McFadden, J., Turin, P., Curtis, D., Magoncelli, A. The electron and ion plasma experiment for FAST. Space Sci. Rev. 98, 33–66, 2001.

Ergun, R., Carlson, C., McFadden, J., Mozer, F., Strangeway, R. Parallel electric fields in discrete arcs. Geophys. Res. Lett. 27, 4053–4056, 2000.

Fälthammar, C.-G. Magnetic-field-aligned electric fields. ESA J. 7, 385–404, 1983.

Fennell, J., Gorney, D., Mizera, P. Auroral particle distribution functions and their relationship to inverted Vs and auroral arcs, in: Akasofu, S.-I., Kan, J. (Eds.), Physics of auroral arc formation. AGU, pp. 91–102, 1981.

Frey, H., Lieb, W., Bauer, O., Höfner, H., Haerendel, G. CCD-camera system for stereoscopic optical observations of the aurora, in: Current developments in optical design and engineering VI. Vol. 2863 of SPIE Proceedings. SPIE, pp. 460–466, 1996.

Gorney, D., Clarke, A., Croley, D., Fennell, J., Luhmann, J., Mizera, P. The distribution of ion beams and conics below 8000 km. J. Geophys. Res. 86, 83–89, 1981.

Gurgiolo, C., Burch, J. Simulation of electron distributions within auroral acceleration regions. J. Geophys. Res. 93, 3989–4003, 1988.

Kaufmann, R., Walker, D., Arnoldy, R. Acceleration of auroral electrons in parallel electric fields. J. Geophys. Res. 81, 1673–1682, 1976.

Kletzing, C., Scudder, J., Dors, E., Curto, C. Auroral source region: plasma properties of the high-altitude plasma sheet. J. Geophys. Res. 108, 1360, doi:10.1029/2002JA009678, 2003.

Klumpar, D., Möbius, E., Kistler, L., Popecki, M., Hertzberg, E., Crocker, K., Granoff, M., Tang, L., Carlson, C., McFadden, J., Klecker, B., Eberl, F., Künneth, E., Kästle, H., Ertl, M., Peterson, W., Shelley, E., Hovestadt, D. The Time-of-flight energy, angle, mass spectrograph (TEAMS) experiment for FAST. Space Sci. Rev. 98, 197–219, 2001.

Knight, S. Parallel electric fields. Planet. Space Sci. 21, 741–750, 1973.

Lindqvist, P.-A. (Ed.), 2001. Auroral Particle Acceleration. Vol. 26 of Phys. Chem. Earth. Elsevier, proc. 2nd EGS Alfvén Conf., Stockholm, Mai, 1999.

Lu, G., Reiff, P., Moore, T., Heelis, R. Upflowing ionospheric ions in the auroral region. J. Geophys. Res. 97, 16855–16863, 1992.

Lyons, L., Evans, D., Lundin, R. An observed relation between magnetic field aligned electric fields and downward energy fluxes in the vicinity of auroral forms. J. Geophys. Res. 84, 457–461, 1979.

McFadden, J., Carlson, C., Ergun, R.E. Microstructure of the auroral acceleration region as observed by FAST. J. Geophys. Res. 104, 14453–14480, 1999.

McIlwain, C. Direct measurement of particles producing visible auroras. J. Geophys. Res. 65, 2727–2747, 1960.

Mizera, P., Fennell, J., Croley Jr., D.R., Vampola, A., Mozer, F., Torbert, R., Temerin, M., Lysak, R., Hudson, M., Cattell, C., Johnson, R., Sharp, R., Ghielmetti, A., Kintner, P. The aurora inferred from S3-3 particles and fields. J. Geophys. Res. 86, 2329–2339, 1981.

Mozer, F., Hull, A. The origin and geometry of upward parallel electric fields in the auroral acceleration region. J. Geophys. Res. 106, 5763–5778, 2001.

Paschmann, G., Haaland, S., Treumann, R. (Eds.). Auroral Plasma Physics. No. 15 in Space Science Series of ISSI. Kluwer, Dordrecht, 2003.

Pfaff, R., Carlson, C., Watzin, J., Everett, D., Gruner, T. An overview of the Fast Auroral SnapshoT (FAST) satellite. Space Sci. Rev. 98, 1–32, 2001.

Reiff, P., Collin, H., Craven, J., Burch, J., Winningham, J., Shelley, E., Frank, L., Friedman, M. Determination of auroral electrostatic potentials using high- and low-altitude particle distributions. J. Geophys. Res. 93, 7441–7465, 1988.

Reiff, P., Lu, G., Burch, J., Winningham, J., Frank, L., Craven, J., Peterson, W., Heelis, R. On the high- and low-altitude limits of the auroral electric field region, in: Lysak, R. (Ed.), Auroral Plasma Dynamics. AGU, pp. 143–154, 1993.

Temerin, M., Carlson, C. W., McFadden, J. P. The low-altitude extent of the auroral acceleration region in the upward current region as determined by upwardly accelerated ion beams. J. Geophys. Res., submitted for publication.